Journal of Alloys and Compounds 817 (2020) 152774

Contents lists available at ScienceDirect

Journal of Alloys and Compounds

journal homepage: http://www.elsevier.com/locate/jalcom

Investigating bulk mechanical properties on a micro-scale: Micro-tensile testing of ultrafine grained Ni–SiC composite to determine its fracture mechanism and strain rate sensitivity

Alan Xu [a, d, *], Chao Yang [b, c, **], Gordon Thorogood [a], Dhriti Bhattacharyya [a, d]

[a] Nuclear Fuel Cycle Research, Australian Nuclear Science and Technology Organisation, New Illawarra Road, Lucas Heights, New South Wales, 2234, Australia
[b] Shanghai Institute of Applied Physics, Chinese Academy of Sciences, Shanghai, 201800, China
[c] Shanghai Key Laboratory of Advanced High-temperature Materials and Precision Forming, School of Materials Science and Engineering, Shanghai Jiao Tong University, Shanghai, 200240, China
[d] School of Materials Science and Engineering, University of New South Wales, Sydney, New South Wales, 2052, Australia

ARTICLE INFO

Article history:
Received 19 July 2019
Received in revised form
20 October 2019
Accepted 22 October 2019
Available online 3 November 2019

Keywords:
Ni-SiC composite
Micro-tensile testing
Strain rate sensitivity
Ultra-fine grained

ABSTRACT

In this study, in-situ micro-tensile testing technique was used to investigate the mechanical properties of ultrafine grained Ni-3wt% SiC composite the size effect on the mechanical properties of the ultrafine grained Ni-3wt% SiC composite, and to further reveal the reasons for the low ductility of the bulk Ni-3wt %SiC composite. Dog-bone micro-tensile samples were manufactured using a Focused Ion Beam (FIB) milling machine to 15 μm length with a cross sectional area of 5 μm by 5 μm. The micro-tensile samples are pulled in tension at a quasi-static strain rate of 0.000087/s (LSR) and a relatively faster strain rate of 0.011/s (HSR). Analysis of experimental stress-strain plots for the LSR tests measured yield stress, ultimate tensile stress and modulus values that approach values previously reported for bulk/macro-level tensile tests. However, the elongation and fracture energy at the micro-level is approximately half that at the bulk scale. This discrepancy is attributed to the presence of unwanted carbon and silicon oxide impurities ~1.5 μm in diameter which act as stress concentrators especially given their large size relative to the width of the tensile specimens. The composition of these impurities was validated by transmission electron microscopy, and they seem to be the most likely cause of low ductility of the Ni-3wt% SiC composite. In all, the study undertaken here was able to replicate mechanical properties observed at the macro scale as well as reproduce a strain rate effect. Furthermore, the failure mode of Ni-3wt% SiC composite was identified and analysed in detail.

1. Introduction

Some specialized Ni Alloys [1] are candidate structural materials for molten salt generation IV nuclear reactors (MSRs) [2,3] owing to their strong resistance against corrosive molten fluoride salts which are selected as the primary coolant of MSRs [4]. As a potential means of minimising the accumulation of radiation damage, researchers have drawn inspiration from metal-oxide/carbide systems such as Oxide Dispersion Strengthened (ODS) steels [5,6] whose finely dispersed oxides act as sinks for excessive vacancies and interstitials introduced by high energy neutrons/ions displacing atoms from their lattice sites. This will have the resulting effect of reducing the degree of irradiation hardening [7]. In fact, Oono et al. [8] have manufactured Ni-ODS alloys and successfully demonstrated the ability of the ODS to act as defect sinks in Nickel and reduce the severity of the radiation damage [8]. For the molten salt system, it is unfortunately not feasible to use a Ni-ODS as oxide particles dissolve within the salt solution [9]. Therefore, the researchers at the Shanghai Institute of Applied Physics (SINAP) have created a Ni–SiC composite, replacing oxide particles with more chemically inert SiC particles [10,11]. The method of manufacturing an ultrafine grained Ni–SiC alloy with grain size about 0.8–1.2 μm

* Corresponding author. Nuclear Fuel Cycle Research, Australian Nuclear Science and Technology Organisation, New Illawarra Road, Lucas Heights, New South Wales, 2234, Australia.
** Corresponding author. Shanghai Institute of Applied Physics, Chinese Academy of Sciences, Shanghai, 201800, China.
E-mail addresses: Alan.Xu@ansto.gov.au (A. Xu), yangchao1987@sjtu.edu.cn (C. Yang).

https://doi.org/10.1016/j.jallcom.2019.152774
0925-8388/

and fine dispersions of about 30–60 nm SiC particles has been developed by Y.Chao et al. who characterised the bulk mechanical properties and high-temperature stability of Ni–SiC composites [12]. Additionally, Huang et al. [13,14] have irradiated Ni-1wt%SiC composites with He ions and found a reduction in volume fraction of Helium bubbles as compared to pure Ni, thus demonstrating the capability of Ni–SiC composites in mitigating irradiation damage.

However, as Ni–SiC is a novel material created at SINAP its mechanical performance under irradiation has yet to be characterised. The authors propose ion irradiation as a means of inducing radiation damage since it is a time and cost efficient means of simulating the radiation damage expected under molten salt reactor conditions [15] (typically measured as displacement per atom, dpa). Nevertheless, one of the drawbacks of using ion-irradiation is the limited penetration depth of ions which is in the range of a few hundred nm - ~15 μm [16]. Such shallow damage depths do not allow for extraction of samples to measure tensile properties by macro scale mechanical testing. Therefore, researchers instead make use of micro-mechanical testing methods to determine mechanical properties of materials post ion irradiation [16–20]. Whilst there are many micro-mechanical testing methodologies, micro-tensile testing offers a direct derivation of the yield stress and elongation of material before and after irradiation. This paper reports on the direct measurement of the tensile properties of this material by *in situ* micro-tensile testing. Thus far, there are relatively few studies on micro-tensile testing of materials, probably due to the time and expendable resources (viz. Ga ions) required for such tests. Kiharra et al., Vo et al., Reichardt et al. and Xu et al. [17,21–23] have investigated slip behaviour of single crystals Ni and 304 stainless steel and determined their slip behaviour, elongation and yield stress. However, the yield stress measured does exhibit size effects which can be corrected for by using a Taylor factor when approximating bulk properties [23]. In this case, the sample size-effect could be overcome due to the fine grain-size since there are more than 25 grains in the cross-sectional area (Yang et al., [24]). Such micro-tensile studies on ultrafine grained samples are unavailable in the literature to date. Thus, apart from directly measuring the tensile properties of the material, this paper will also help in validating the hypothesis of grain-size domination of mechanical properties for this material, when the sample size is a few microns. Moreover, this study will also serve to determine the comparability of micro-scale tensile tests with macro-scale tests.

As mentioned above, the authors use *in situ* micro-tensile testing to directly probe the tensile properties of this material to establish base-line properties and to determine the suitability of this technique for studying the Ni–SiC composite in future ion irradiation experiments. Moreover, in testing the ultrafine grained Ni–SiC composite on a micro scale the validity of in-situ micro-tensile tests can be evaluated against literature on bulk samples [11]. Additionally, we test the micro-tensile samples at different strain rates to measure the strain rate sensitivity and compare with literature values on polycrystalline pure Ni of similar grain size. This will also help in benchmarking the extent of variations in the tensile test results that may be obtained by testing at strain rates differing by up to two orders of magnitude, though all being in the quasi-static regime. Thus, it should be helpful in comparing results from, say, different research institutions doing tests at different strain rates. Finally, we use Electron Back Scattered Diffraction (EBSD) combined with TEM analysis to determine the failure mechanism and influence of SiC particles on mechanical properties. The work reported here will also serve as a reference point for future tests of irradiated Ni–SiC alloys currently being undertaken at Australian Nuclear Science and Technology Organisation (ANSTO) and SINAP.

2. Experimental methods

In this paper we study a Ni-3wt.% SiC composite manufactured in the research laboratory at SINAP and previously characterised and reported in the papers [12,25]. Ni powder was initially mixed with SiC in a planetary ball mill and grounded for 48 h until it reached a fine particle distribution [12]. After milling, the samples were compacted and sintered using a spark plasma sintering (SPS) furnace (Germany, KCE-FCT-HP D 25/4-SD ®) producing a densified cylindrical ingot of 52 mm diameter and 12 mm height [12]. Studies of the grain size and morphology of the sintered ingot cross-section using EBSD found a uniform distribution of equiaxed grains 0.9 μm (average) in diameter. Transmission electron microscopy (TEM) revealed uniformly distributed SiC particles of 250 nm (average) diameter [12]. Thus, the sintering conditions used did not introduce any non-uniform grain growth and the resulting density is high measuring 98.5%.

A new batch of Ni-3wt%SiC was manufactured by SINAP for this study, using the same aforementioned processing methodology. Dog-bone samples were fashioned from this batch of Ni-3wt%SiC with dimensions of 2.5 mm × 1 mm cross section area and gauge length 12 mm using wire cutter. The samples were tested at low strain rate of $0.0007s^{-1}$, a quasi-static strain rate via a Zwick Amsler 100 HFT 5100 tensile testing machine at SINAP. The new batch of Ni-3wt.%SiC were also prepared for micro-tensile testing at ANSTO. A 0.5 mm thick square slice, 7 mm by 7 mm in breadth and width was cut from a cylindrical ingot via wire cutting. This sample was then wax mounted on a sample stub and grounded from 120 grit to 4800 grit SiC pad followed by progressively finer diamond pad polishing using a coarse cloth pad and diamond grades 15 μm, 6 μm–1 μm spending 30–45 min per grade. A final 50–100 nm colloidal silica polish of the sample for 1 h achieved a smoothly polished and flat surface free of any μm sized scratches. The as-polished sample was then wax mounted on to a dovetailed aluminium stub specially designed for both insertion into the micro-tensile testing rig and the Focused Ion Beam (FIB) milling machine. A Zeiss® Auriga 60 Cross beam™ FIB at ANSTO was used to fashion 5 μm wide and 15 μm long dog-bone samples from one of the edges of the sample using an initial rough milling current of 20 nA followed by finer milling currents of 4 nA and 1 nA. An undercut was then performed on the orthogonal side face of the sample to reduce the thickness of the dog-bone samples to 5 μm depth, thus giving it a square 5 × 5 μm square cross-sectional area. To minimise stress concentrations, 3 μm radius fillets were introduced where the tensile sample was connected to the sample substrate and also where it connected to the rectangular head to be pulled by the gripper in the micro-tensile testing rig. The gripper which was used to pull the dog-bone samples was made of tungsten. It was pincer shaped and 20 μm thick. It featured a smooth vertical face with which to engage and pull the rectangular head of the sample as shown in Fig. 1 below, which was a top view Scanning Electron Microscopy (SEM) image of the gripper next to the dog-bone sample. Previously, Reichardt et al. [22] adopted a similar grip shape for testing 1 × 1 μm square cross-sectional area dog bone samples, obtaining results of high accuracy and reliability. Also shown in Fig. 1 are the fiducial markers, lightly milled at 120 pA onto each end of the sample which was used to measure sample strain from their SEM images taken during the tensile tests.

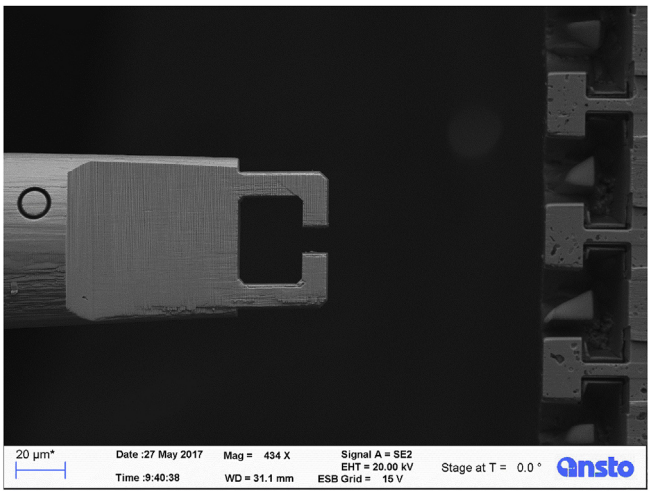

Fig. 1. Top view, 20 kV Scanning Electron Microscope (SEM) image of the tungsten pincer gripper and dog-bone sample manufactured by FIB milling.

The dog-bone samples were tested under tension in a micro-tensile testing rig designed and supplied by MicroTesting Solutions® pty ltd. The testing rig, along with the samples, was mounted in a Zeiss UltraPlus SEM which allowed for imaging of the sample at 20 kV as it is being strained. The gripper is attached to a piezo-electric stage which moved it along one dimension only: either forward or backward depending on the voltage applied to the piezo. The sample was mounted on a stage with 3 dimensions of movement, allowing for slight adjustments for sample alignment. Once the sample head mated with the interior grip faces (Fig. 1), the voltage on the piezo decreased, causing the grip to move backwards and thus pulling the dog-bone sample in tension. The displacement rate of the grip (specified in nm/s) controlled the strain rate experienced by the sample. 5–6 samples were tested for each strain rate: 0.000087/s and 0.011/s. The former will be referred to as Low Strain Rate sample (LSR) and the latter as High Strain Rate sample (HSR) henceforth in this paper. As the tensile test took place, the load experienced by the grip was recorded and was converted into engineering stress by dividing through by the initial sample cross-sectional area. Additionally, the displacement of the gripper is also recorded, an indirect measure of the sample displacement. The gripper displacement can be converted into the sample strain by a linear relationship that exists between grip displacement and sample strain (measured by displacement of fiducial markers placed at either end of the dog-bone sample) in the SEM images as taken at 0.1–0.5 µm intervals. Appendix 1 shows the graphical plot of grip displacement vs engineering strain measured from SEM images accumulated across three samples at 0.000087/s attaining a high correlation value of above 99% when a linear relationship is assumed. The data points obtained via either route are merged together to obtain a complete engineering stress-strain graph. Furthermore, taking an SEM image of the sample in tension is only done for tests where the quasi-static strain rate of 0.000087/s is applied as it involves momentarily stopping the gripper for 10 s to take a high-resolution image. If high resolution SEM images are taken at regular intervals for the non-quasi-static strain rate: 0.011/s then the stress-strain response recorded becomes inaccurate. This is because the test is paused to take SEM images which reduces the average strain rate experienced and introduces stress-relaxations and creep of the sample. Thus, at the non-quasi-static strain rates, SEM images are not taken during testing and the relationship detailed in Appendix 1 is used to infer the sample strain from the gripper displacement. However, this relationship in Appendix 1 is only valid for the plastic deformation region of the stress-strain curve (from the 0.1% proof stress onwards) as the strain measurements from images become inaccurate for the elastic region. As a result, for stress-strain plots of 0.011/s samples, the linear elastic region is artificially inserted from the 0.000087/s tensile samples. It is a reasonable approximation as it is known that a material's modulus does not change with strain rate.

EBSD and Energy Dispersive X-ray (EDX) mapping is performed on the batch of Ni-3wt%SiC to determine its grain and particle size using an Oxford® NordlyS™ Detector attached to the same Zeiss UltraPlus SEM mentioned earlier. They were also used to map micro-tensile dog-bone samples pre- and post-tension testing. Additionally, for two of the 0.000087/s, quasi-static tension tests, the test is stopped when the sample stress is 20–40 MPa below the UTS and the EBSD and EDX at the intermediate stage of deformation is obtained before carrying on with the tensile test. All the data are analysed using the Oxford® Aztec™ and Channel 5™ software packages.

Additionally, the Zeiss® Auriga 60™ FIB was used to manufacture TEM samples from the as deformed tensile samples to study the fracture region in greater detail. Initially, a rough milling current of 30 kV 4 nA was used to mill out a trench around a platinum deposited rectangular strip 2 µm by 10 µm in area and then finer 30 kV 1 nA milling current used to undercut the rectangular slice and create a free hanging cantilever. An Omniprobe™ micromanipulator was inserted and the tungsten tip was welded onto the free hanging end of the cantilever by platinum deposition prior to the cantilever being cut and freed from the surface. The cantilever was then attached to a 3 mm copper half grid post using platinum deposition and the tungsten tip was detached. Successively finer currents of 30 kV 240, 120, 50 and 10 pA were used to reduce the cantilever into a thin slice ~100 nm thick with final 2 kV 240 pA milling used to reduce any gallium damage. The samples were then analysed in a Jeol® 2100 FS™ TEM at 200 kV under two beam bright field and dark field modes to analyse the dislocations within the longitudinal cross-section of the sample.

3. Results

3.1. Microstructural characterization through SEM

EBSD coupled with EDX mapping was performed on an as polished Ni–SiC composite sample analysed at 20 kV and at 70-degree tilt on a 150 by 140 µm area using a step size of 200 nm. The inverse pole figure (IPF) orientation map relative to the x-axis (x-axis being parallel to the scale bar), carbon, silicon and oxygen composition maps for this sample are shown in Fig. 2a, b, c and d respectively. The line intercept method was used to measure the size of the grains in Fig. 2a and it was found to be 1.5 ± 0.4 µm which approaches the literature values reposted earlier. Upon examining Fig. 2b-d, it is apparent there are anomalously large precipitates present having diameter of 1.57 ± 0.07 µm which are much larger than the SiC precipitate size with a diameter of 265 nm expected for this alloy [12]. Moreover, these large precipitates are predominantly Carbon, being devoid of Silicon indicating that they are not SiC precipitates. There is also another type of equally large particles 1.52 ± 0.08 µm diameter composed of Silicon and Oxygen but devoid of Carbon suggesting they are not SiC particles either. Furthermore, regions high in Carbon do not coincide with the regions high in Si which indicates that they formed independently of each other and they are likely impurities introduced possibly in the

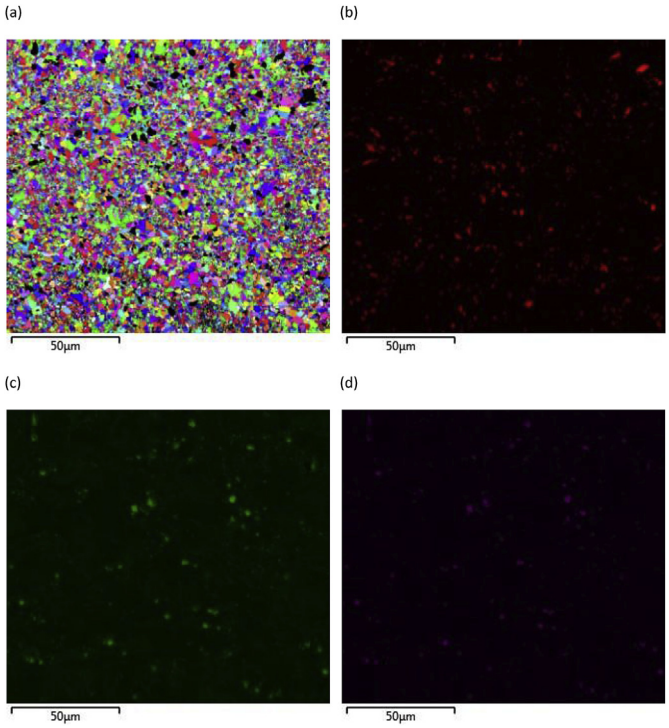

Fig. 2. (a) Inverse Pole Figure of grain orientation along x axis (parallel to the scale bar) of Ni–SiC composite at 20 kV, 70° tilt and 200 nm step size. Corresponding EDX map showing (b) Carbon, (c) Silicon and (d) Oxygen.

early particle milling process. Digital image analysis of the EDX images found the area fraction for the Carbon particles to be 6.8% whilst the Silicon–Oxygen particles to be 1.3%. So, the total impurity particle area fraction equals 8.1%. The large size of these particles relative to the size of the tensile test specimens is expected to reduce the ductility of the micro-tensile samples as elaborated in detail in the following two sections. The batch of Ni-3wt%SiC provided by SINAP for this study certainly deviates in quality from early batches studies in Refs. [12,25]. Despite this, the authors continue to study this batch to determine how large impurities may affect the materials mechanical properties on a micro and macro scale. Finally, it is important to note that the ultra-fine SiC precipitates are still present within the micro-structure and identified in TEM analysis later on in this section, however, they evade detection in this SEM EDX map owing to their small size and the large interaction volume of the 30 kV electron beam [12].

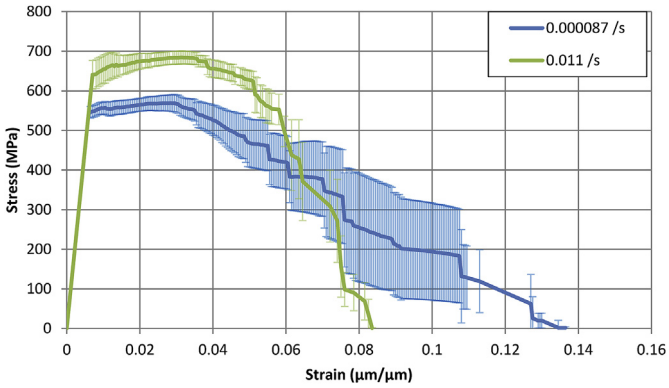

Fig. 3. Stress strain plots of Ni–SiC alloy tested at 0.000087 and 0.011/s, each plot an average of 5–6 samples.

3.2. Effect of strain rate on hardening response

The engineering stress-strain plots for Ni–SiC samples tested at low and high strain rates of 0.000087 and 0.011/s are displayed in Fig. 3. Each plot is calculated by averaging across 5–6 micro-tensile tests and the error bars shown are calculated from the standard deviation at each data point divided by the square root of the sample size beginning from the Yield Stress (YS), that is, the 0.1% proof stress. The average Young's Modulus for the LSR samples was measured to be 90.3 ± 7.1 GPa and it is artificially inserted for the HSR plot in Fig. 3 (see Experiment section for explanation). Comparing between the LSR and the HSR samples, the strain rate effect is statistically evident as the plots are outside of each other's error ranges with the stress of the HSR being roughly 100 MPa higher than the LSR up to 0.3 strain (the UTS of the LSR plot). The HSR test featured a smaller elongation to failure than the LSR sample which is expected of sample tested at relatively higher strain rates. For both 0.000087 and 0.011/s samples, the error ranges become very large and overlap each other beyond the UTS. It can be attributed to the presence of anomalously large precipitates which are comparable in size to the width of the dog-bone samples: 5 μm. Thus, the volume fraction of precipitates within the dog-bone sample volume: 5 × 5 × 15 μm can have high degree of variability in volume fraction and number density. The elongation and necking behaviour of the micro-tensile samples will have greater degree of variability because of this as evident in Fig. 3.

To further validate and quantify the plots in Fig. 3, the elongation to Ultimate Tensile Stress (UTS) and Failure are averaged for the LSR and HSR tests and listed in Table 1. Also listed in Table 1 are the averaged YS, UTS and Fracture Energy, which is calculated from the area underneath each stress-strain plot. The values presented in Table 1 are calculated in a different manner to Fig. 3, as Table 1 values of strain and stress are averaged from the elongation and yield for individual plots, whilst stress strain plots in Fig. 3 is created through averaging the stress at each strain value. Thus, Table 1 gives a more accurate presentation of values while Fig. 3 provides more of a qualitative graphical visualisation. Regardless, the elongation data in Table 1 further validates what is observed in Fig. 3 as the elongation for the LSR strain rate test is longer than the HSR tests. Moreover, the YS and UTS are both statistically higher at HSR by ~100 MPa compared to the LSR tests. It is also interesting that the strain to UTS is 3–4 times smaller than the strain to failure which shows the samples do have limited ductility and spend more strain necking. Further, Table 1 shows that the fracture energy for both samples are within each other's error ranges indicating strain rate has no effect on the energy required to pull the samples to failure. This observation along with others observations noted thus far highlight the similarity in the strain rate behaviour observed at micro scale as compared to what is typically observed for macro-scale samples [26].

3.3. Comparison of micro and macro scale quasi-static tensile tests

In Fig. 4, the aforementioned micro-scale scale test result for LSR is plotted against the macro-scale test (sample size: 2.5 mm × 1 mm cross section area and gauge length 12.5 mm) also tested at a quasi-static strain rate: 0.0007/s. The two plots for micro and macro scale test show very similar modulus and yield stress with the values largely overlapping each other in the region between YS and UTS. This is supported quantitatively in Table 2 which compares the measured mechanical properties of the micro-scale (data reproduced from Table 1) and macro-scale test (reproduced from Ref. [25]). The measured elastic modulus, yield stress and

Table 1
Sample Elongation, Yield Stress, Ultimate Tensile Stress and Fracture energy for 0.000087 and 0.011/s strain rate as averaged across 5–6 samples each.

Strain Rate	Strain To UTS (μm/μm)	Strain To Failure (μm/μm)	Yield Stress (MPa)	Ultimate Tensile Stress (MPa)	Fracture Energy (MJ/m3)
0.000087/s	0.026 ± 0.011	0.0948 ± 0.0132	544.99 ± 14.66	588.46 ± 24.77	42.97 ± 8.21
0.011/s	0.0191 ± 0.0053	0.0704 ± 0.003	640.61 ± 32.85	702.58 ± 21.06	39.63 ± 1.67

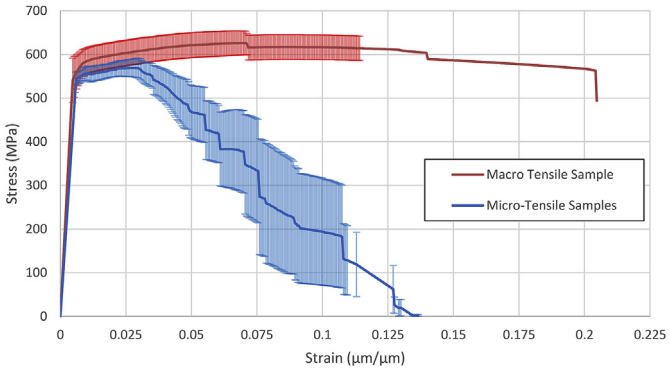

Fig. 4. Engineering stress-strain plot for micro and macro scale tensile tests of Ni–SiC composite.

ultimate tensile strength for the micro and macro tension tests are within at most 5% of each other's values indicating a close agreement between the two methods. However, the elongation and fracture energy of the micro and macro tensile tests are significantly reduced in the micro-scale test being a little more than half compared to the macro-scale test. Thus, there is a reduced ductility in the micro-test compared with the macro test.

3.4. Role of impurity particles on mechanical properties

During the manufacturing of the micro-tensile samples, sites were chosen at random with some of the fabricated micro-tensile samples featuring large carbon particles ~1.5 μm in diameter. One such micro-tensile sample featuring two large carbon particles on its surface is shown in Fig. 5a as imaged in SEM at 20 kV before it was tested at a strain rate of 0.000087/s. The corresponding EBSD Inverse Pole Figure (IPF) plot relative to the x-axis (the tensile axis of the sample) and the local misorientation map (legend is units of degrees) are also displayed in Fig. 5a. Similarly, Fig. 5b shows the SEM image and EBSD map of the same sample pulled to a stress of 568 MPa, just below the UTS of the sample while Fig. 5c shows the SEM image, EBSD map and local misorientation map of the sample post fracture.

It is immediately apparent the majority of the deformation is concentrated around the two large precipitates. Between Fig. 5a and b, the majority of grain rotation and local misorientation appears to have occurred for the grains which are circled in Red in Fig. 5a–c with the sample subsequently fracturing within this region shown in Fig. 5c. Within this circled region, we see three grains adjacent to a large impurity particle that undergo a considerable degree of rotation as evident when comparing between Fig. 5a and b. Moreover, the greatest amount of local misorientation is also concentrated in the region circled in Red. In Fig. 5a, the green coloured grain adjacent to the carbon-rich particle is oriented with the $[2\ \bar{1}\ 0]$ direction parallel to the tensile direction, which rotates to $[5\ \bar{1}\ \bar{1}]$ direction as the tensile stress approaches the UTS in Fig. 5b (This rotation results in the IPF map in Fig. 5b. to show the grain as red) The grain was measured to experience a rotation of 78°, which is significantly higher than the rotation experienced in the two light-blue coloured grains of 7.75°. These two light-blue coloured grains are adjacent to the green coloured grain and the carbon-rich particle in Fig. 5a. They are originally oriented along $[5\ 2\ \bar{4}]$ direction before testing and rotate into the $[5\ 3\ \bar{4}]$ direction as the tensile

Table 2
Mechanical properties: modulus, elongation, yield stress, ultimate tensile stress and fracture energy of Ni–SiC composite (data sourced from Ref. [25]).

	Young's Modulus (GPa)	Elongation To UTS (μm/μm)	Elongation To Failure (μm/μm)	Yield Stress/YS (MPa)	Ultimate Tensile Stress/UTS (MPa)	Fracture Energy (MJ/m^3)
Micro Scale Test	90.9 ± 7.3	0.026 ± 0.011	0.095 ± 0.013	544.99 ± 14.66	588.46 ± 24.77	42.97 ± 8.21
Macro Scale Test	116.1 ± 22.3	0.076 ± 0.007	0.134 ± 0.039	540.63 ± 50.78	627.67 ± 27.00	89.64 ± 18.99

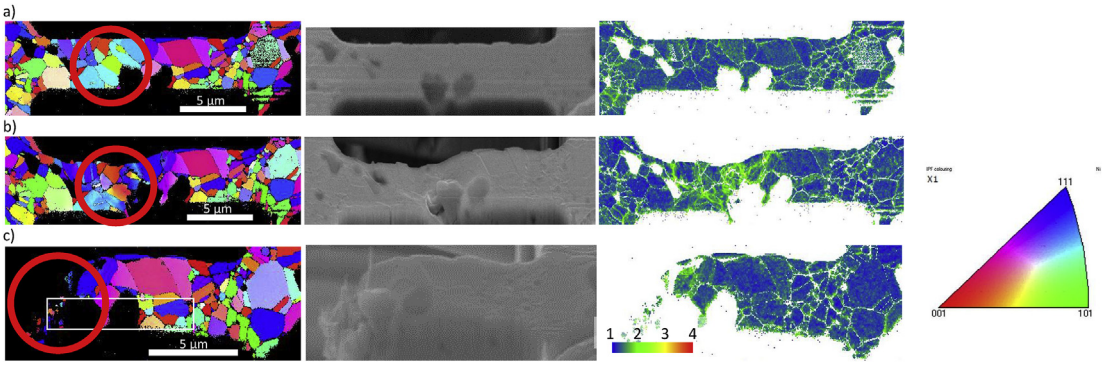

Fig. 5. EBSD IPF colouring maps with respect to the tensile direction (x-axis) for a tensile sample with large precipitates present on its surface at three different stages of testing: (a) pre-testing (b) at the ultimate tensile stress (insert stress here) and (c) post fracture. The Local misorientation maps for each of the corresponding testing states shown at their right.

stress nears the UTS in Fig. 5b. The reason for the difference in grain rotation can be explained by the difference in Schmid factor between the green and light-blue coloured grains. The green coloured grain had a higher Schmid factor of 0.490 as compared to 0.445 for the light-blue coloured grains so the resolved shear stress within the green coloured grain is higher and thus it deforms at a lower stress and to a greater extent than the light blue coloured grain [23,27]. Similarly grains within the red circled region which are purple or red, being close to the [1 0 0] or [1 1 1] crystal direction experiences the least amount of crystal rotation as their Schmid factor are the lowest relative to the light blue and green coloured grains. In Fig. 5c, the fracture has occurred adjacent to the carbon-rich particle seemingly transgranularly across the green and light-blue grains Appendix 2 shows the pole figure plots for the aforementioned green and light blue coloured grains. The pole figure plots show a greater degree of rotation for the green grain (X' pole in {110}) as compared to the light blue grain.

3.5. Fractographic analysis

The tendency for the micro-samples to fail near large precipitates or impurity particles is consistently observed across the samples tested. Fig. 6a and b show another two tensile samples tested at LSR and 0.011/s where the sample has failed near the

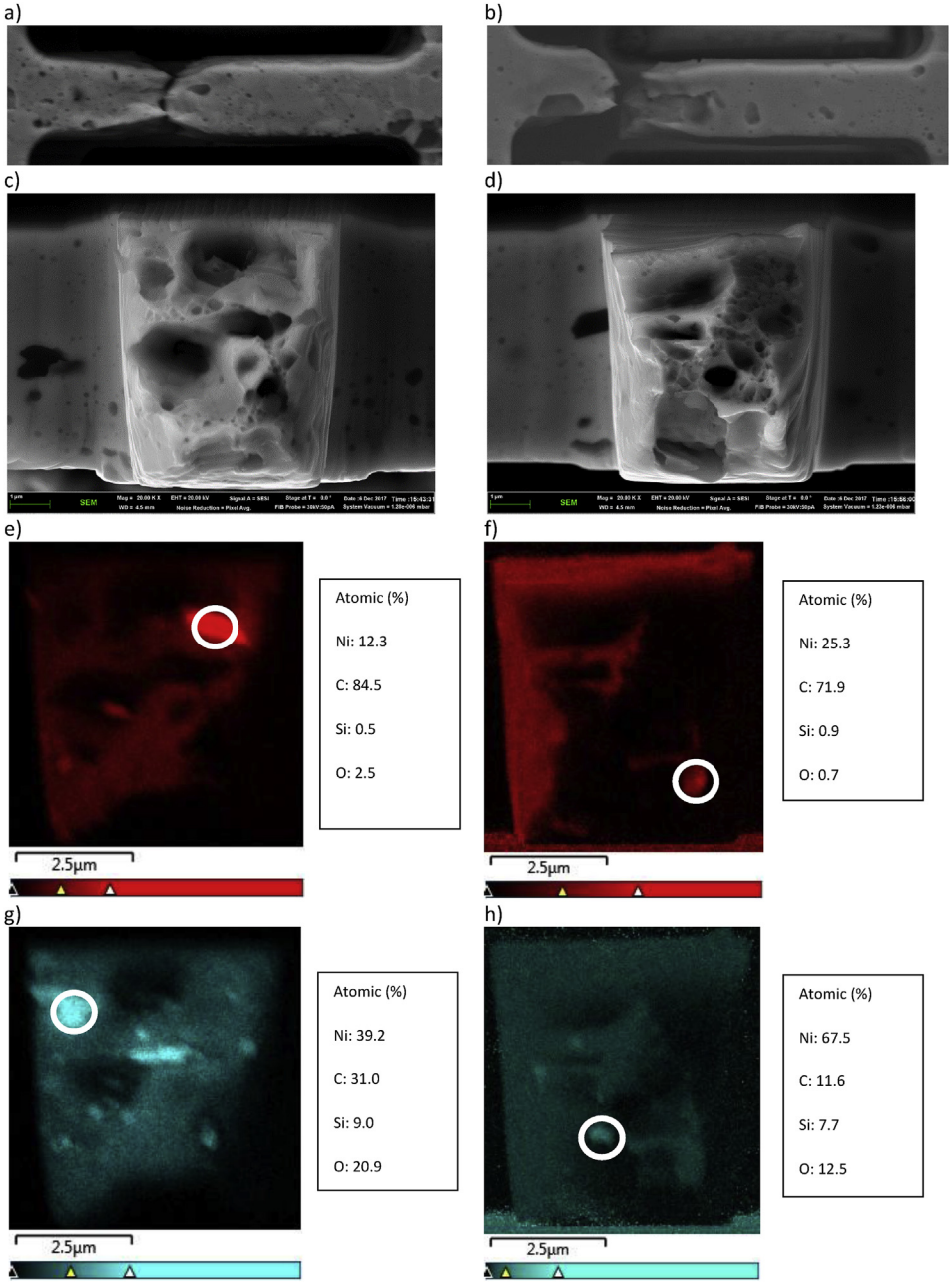

Fig. 6. Top view SEM image of As fractured NiSiC alloy dogbone samples tested at strain rate of (a) 0.000087 and (b) 0.011/s containing large impurity/precipitate on the surface. Corresponding SEM image of the fractured surface of the samples for (c) 0.000087 and (d) 0.011/s. EDS analysis of the fracture surface of Fig. 5a,c showing the chemical maps for (e–f) C and (g–h) Si.

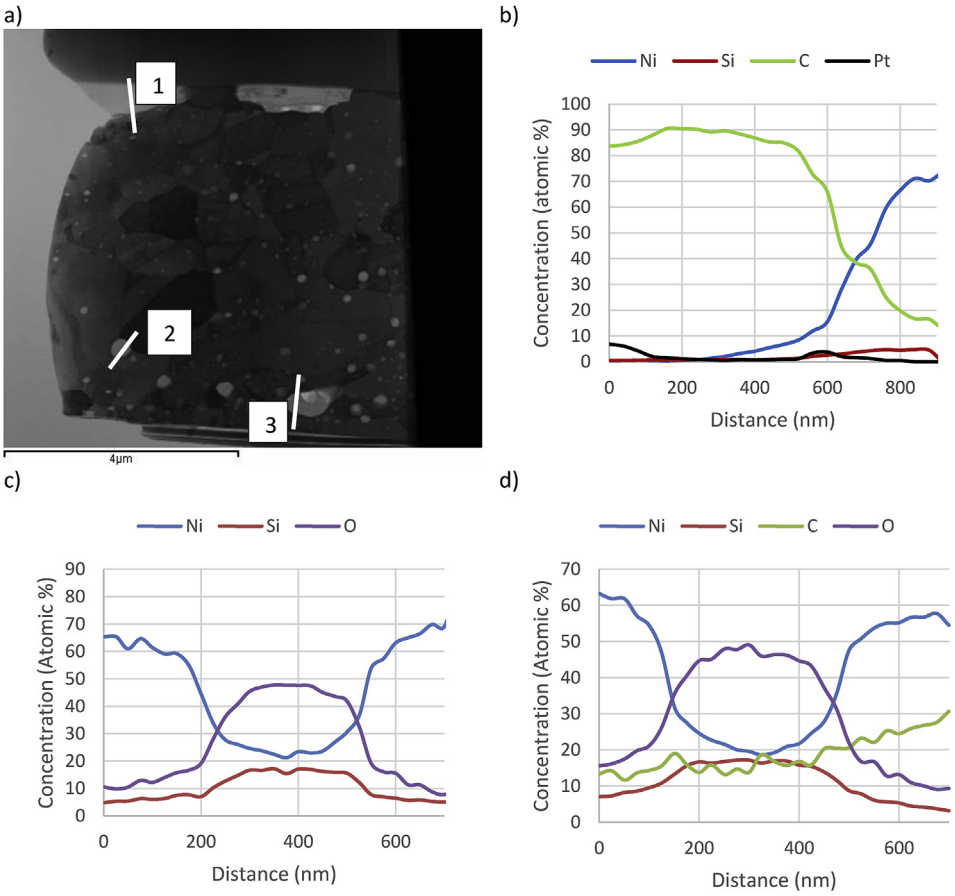

Fig. 7. (a) STEM brightfield image of Ni 3 wt% SiC composite taken from as deformed micro-tensile sample. EDS line scan showing composition profiles of particles labelled 1, 2 and 3 are plotted in b), c) and d) respectively.

precipitates. The corresponding fracture surfaces for the samples are shown in Fig. 6c and d respectively. Some parts of the fractured surface are covered in fine dimples indicating it failed by void coalescence, a ductile failure mechanism typical of Ni as noted by Wang et al. [28,29]. However, there are also large and deep cavities 1 μm in diameter with flat rather than curved surfaces indicating local brittle fracture has taken place and the overall fracture mode could be a mixture of ductile failure and brittle cleavage. To understand the cause of these deep dimples, EDS analysis was performed on the fracture surface of sample in Fig. 6c and the chemical composition maps for C, Si and O are reported in Fig. 6e and g respectively. Likewise, the EDS composition maps of the fracture surface in Fig. 6d are reported in Figure f) and h) for C, Si and O respectively. Across both samples, the EDS analysis shows the large 1 μm diameter cavities seen on the fracture surface in Fig. 6c-d are usually adjacent to impurity particles high in Carbon, Oxygen and Silicon. The chemical composition of three particles as circled in white are listed adjacent to the elemental maps. It can be seen that some of the particles are high in Carbon while others have high concentrations of Silicon and Oxygen and relatively lower Carbon content. As the EDS chemical map is made from an uneven fractured surface, we concede that the results are more qualitative than quantitative. They serve to highlight where the impurity particles are and show that they could possibly be points of weakness that initiate brittle fracture, which is aligned with the observation made in the previous section.

In order to undertake a more precise EDS analysis of the impurity particles present in the material, a TEM sample was fabricated from the fractured sample previously shown in Fig. 5c. The two large particles at the top of the sample surface in the SEM image (Fig. 5c) correspond to the two particles below the platinum layer at the top side of the TEM image (Fig. 7a). The white rectangle in the SEM image highlights the region from which the TEM sample is made. The Bright Field STEM image of this TEM sample is presented in Fig. 7a. There are white lines numbered 1 to 3 drawn across certain impurity particles of interest from which EDS line scans are created. The EDS line scans for the lines 1, 2 and 3 are shown in Fig. 7b, c and d respectively. The composition profile for line 1 confirms what was observed in the SEM EDS maps in Fig. 6e and f being 85 at% Carbon. TEM convergent beam electron diffraction (CBED) performed on this carbon rich particle further confirmed that its structure is amorphous. The diffraction pattern shown in Appendix 3 shows only a single direct beam spot and no lattice spots or Kikuchi bands present which is characteristic of an amorphous structure. Meanwhile, the line scans in Fig. 7c and d shows these particles are rich in Si and O and are most likely SiO_2 as the ratio of Si to O is 1:2. Thus, in depth TEM EDS analysis further validated what was observed in the SEM EDS analysis. There is strong evidence that impurity particles of amorphous C or silicon dioxide present within the microstructure are sites of stress

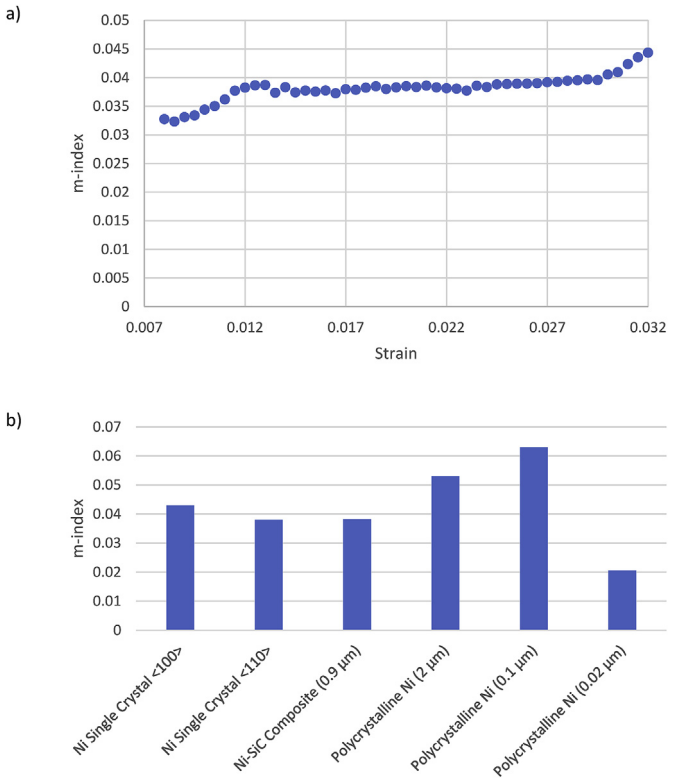

Fig. 8. (a) Strain rate sensitivity index (m-index) calculated for Ni–SiC composite for strain rates of 0.000087 and 0.011/s between yield stress to ultimate tensile stress. (b) The average strain rate sensitivity (m-index) calculated for Ni–SiC composite compared against the m-index calculated for single crystal micro-tensile samples, ultra fine grained Nickel (2 μm) and nanocrystalline Nickel (0.1 and 0.02 μm) reproduced from: [21,26,27].

concentration and embrittle the material.

4. Discussion

4.1. Strain rate effect at the micro-scale

In this study, a strain rate hardening effect was observed as the yield stress and ultimate tensile stress increased between samples tested at a quasi-static strain rate of 0.000087/s and a relatively fast strain rate of 0.011/s. In order to quantify the strain rate effect further, the strain rate sensitivity is calculated for a range of stress-strain values between the yield and ultimate yield stress for the 0.000087/s and 0.011/s strain rate micro-tensile samples. The strain rate sensitivity or m-index is traditionally calculated using the formulation detailed in Equation (1) [30] (s is the engineering stress and ė is engineering strain rate for constant temperature) and the m-index are plotted against strain in Fig. 8a.

$$m = \left[\frac{\ln\left(\frac{s_1}{s_2}\right)}{\ln\left(\frac{\dot{e}_1}{\dot{e}_2}\right)}\right] \quad (1)$$

Upon examination, the m-index for the Ni–SiC composite appears to plateau at an average value of 0.038, indicating the ratio in stress between the 0.000087 and 0.011/s strain rate samples remains fairly constant during the work hardening regime. This is a strong indication that strain rate effects can be reliably ascertained at the micro-scale. Furthermore, Fig. 8b compares the m-index for the Ni–SiC samples against other m-index values reported in literature for various pure Ni samples. The two data points to the left of the Ni–SiC data point are the m-index for single crystal Ni also tested at the micro-scale. The data, as reproduced from Xu et al. [23] show the m-index values measured for crystal directions of <100> and <110> are 0.043 and 0.038 respectively. The values closely approach the m-index for Ni–SiC composite measured here which seem to suggest the SiC precipitates and various impurity particles do not have a huge effect on the m-index. Further support for this observation can be found when we compare the m-value against literature values for macro-scale tests of pure Ni polycrystalline which are the three data points to the right of the Ni–SiC data point in Fig. 8b. The m-index for ultra-fine crystalline (2 μm) and nanocrystalline (0.1 μm) Ni are reported to be 0.053 and 0.063 respectively as sourced from Humphreys et al. [31]. Meanwhile, Schaiwger et al. [32] reported a m-index of 0.021 for 0.02 μm diameter nanocrystalline Ni. Thus, the m-index obtained for Ni–SiC composite at the micro level appears to fall within the range of values reported in the literature for macro scale pure Ni crystals of different grain sizes. This is in spite of the presence of impurities and precipitates in the Ni–SiC composite compared to the pure Ni. The results along with previously published results in Ref. [23] show strain-rate sensitivity can be reliably ascertained at the micro scale. It is a novel discovery as this topic has not been very thoroughly investigated for micro-tensile testing.

Moreover, it appears that grain size exhibits minimal effect on the strain rate sensitivity at relatively large grain sizes, since the m-index is approximately the same in the present case (greater than~ 1.6 μm in Ni-3wt%SiC) as in the previous single crystal tests (with sample size ~ 12 × 12 μm^2). The findings are in general agreement with studies by Humphreys et al. [31] where the authors noted the m-index increases for the grain size range 26 nm to about 2 μm. At large grain sizes, the size of the burgers vector relative to the distance from grain boundaries is relatively small so stress fields around grain boundaries have negligible effect on the m-index. However, where the grain size approaches 26 nm, the interaction between dislocations and grain boundaries become more dominant. Greater activation energy is required to initiate dislocation motion and so the strain rate sensitivity increases.

4.2. Work hardening behaviour of micro and macro tensile samples

Trend line fitting of the hardening curves in Figs. 3 and 4 using the traditional work hardening equation (Equation (2)) [30] allows the materials parameters: strength coefficient, K, and strain hardening exponent, n to be derived. The other parameters in Equation (1): s, ė, m and e are engineering stress at strain e, strain rate, strain rate sensitivity and engineering strain respectively. As we know s_{ys}, ė and m to be constants, we plot stress against strain and apply Equation (2) in order to derive the aforementioned K and n values. Equations(3)and(4) are the work hardening equation as derived for micro-tensile tests of the Ni–SiC composite at strain rates of 0.000087 and 0.011/s respectively (from Fig. 3). Equation (5) is the work hardening equation derived for the macro-scale quasi-static tensile test plotted in Fig. 5. The strain rates and the m-index are previously reported in §2 and §4.1

$$s = K\dot{e}^m e^n \quad (2)$$

$$s = 618.5 \times (0.000087)^{0.038} \times e^{0.0214} \quad (3)$$

$$s = 738.5 \times (0.011)^{0.038} \times e^{0.0208} \quad (4)$$

$$s = 640.3 \times (0.0007)^{0.038} \times e^{0.0262} \quad (5)$$

In comparing Equation (3) (0.000087/s) with Equation (4) (0.011/s), the strength coefficients are very close to each other which is expected as it is a constant dependent solely on the material itself. The only difference between the equations lay in the strain hardening exponent, n, which is higher for the low strain rate than for the higher strain rate tests. This again agrees with literature predictions for metals in general. In fact, such phenomenon has been observed for a BCC phase Ti60 alloy by Luo et al. [33] where the strain hardening exponent also decreases as a result of strain rate increase, in agreement with the trend observed here. Luo et al. explained the behaviour in terms of dislocation activation energy which is lowered at higher strain rates enabling greater mobility and hence resulting in a lower n value. Such behaviour is also expected to occur in FCC structures as detailed by Abbaschian et al. [34] and is the underlying mechanism across both crystal structures. The findings of Luo et al. involve testing at a much higher temperature of 947–1057 °C whilst the Ni-3wt%SiC test took place at room temperature (25 °C) so it would be difficult to compare the strain hardening-strain rate relationship quantitatively. Perhaps a future study would be to investigate the change in n with strain rate across different crystal structures.

In a different study on BCC metals, Ding et al. [35] investigated the change in strain rate sensitivity with grain size for pure iron samples within a grain size range of 0.9–25 μm at room temperature. Ding et al. noted the m-index for iron increases as the grain size increases which contrasts the behaviour seen in FCC Nickel. The difference can be explained by the different deformation mechanism between iron and nickel. At room temperature, iron deform predominantly via screw dislocation which have low mobility and are strongly strain rate sensitive [35] whilst nickel deform through edge dislocation which are relatively less strain rate sensitive. Nonetheless, the fact we can reproduce a strain rate induced deformation behaviour that meets literature predictions for macro-scale metals highlights the accuracy and reliability of micro-tensile testing in undertaking mechanical investigations of metals.

Meanwhile, in comparing Equation (3) (LSR, micro-tensile test) to Equation (5) (0.0007/s, macro-scale tensile test), there is high similarity in the K and n values reported. The micro-scale test differed from the macro-scale test by 3.4% with regard to the K value and 0.9% for the n value. Thus, it appears we are reproducing the same hardening behaviour at the small micro-scale as at the macro scale. The result achieved here is supported by studies of Yang et al. and Gu et al. [24,36,37]. The researchers found through studying micro and macro sized compression/tensile samples of differing grain size, that sample size effect dominates when the ratio of sample diameter to grain size falls below 5 (less than 25 grains in cross sectional area). For the Ni–SiC sample the sample diameter to grain size ratio is higher than 5 and the fact we can replicate macro-scale hardening behaviour and yield stress at the micro-scale is a testament to the effect of that.

4.3. Effect of impurity particles on Ni–SiC composite

However, the micro-tensile test is not without limitations as effects of local imperfections and impurities can be amplified at the micro-scale where it is supressed at the macro level due to an averaging effect. In Fig. 3 and Table 1 the elongation measured at the micro-scale is approximately half that of the macro scale samples. The premature failure of micro-scale samples is attributed to the presence of large impurity particles identified as amorphous C and SiO_2 via TEM EDS analysis (Fig. 7a–d), averaging 1.5 μm in diameter and having a total area fraction of 8.1%. It is likely that these impurity particles amplify stress locally as their size is comparable to the width of the micro-tensile samples. As shown in Fig. 5a-c, the tensile sample has two large impurity particles present having a local area fraction of 12.5% which is far greater than the 8.1% measured for this sample in the macro scale. These impurities are proven to be points of failure for micro-scale tensile tests as the EBSD maps in Fig. 5a-c show that the majority of grain deformation and rotation occurs adjacent to the impurity particles. It is further evidenced in the fractographic analysis in Fig. 6a-h of two additional micro-tensile samples. EDS analysis of the fractured surface consistently reveals fine dimples within grains indicating ductile intragranular failure but appears to be cleaved at regions near impurities, a sign of brittle precipitate-grain interface fracture. Similarly, the preferential failure of the micro-tensile samples near particles revealed the failure mechanism of the Ni–SiC composite. It could possibly explain why macro-scale tests Ni–SiC has such a low failure strain of 13.4% as compared to previous batches without impurity particles whose failure strain is 16%. There is a 3% reduction in ductility as a result of the presence of impurity particles and micro-tensile testing helped uncover the underlying reason for this. Because of the chance occurrence of impurity particles in some micro-tensile samples, and therefore their significantly higher area/volume fraction in these samples, they affect the elongation of these micro-tensile samples more severely than that of macro-tensile samples.

5. Conclusions

In this study, micro-sized dog-bone samples of Ni–SiC composite were fabricated by FIB and tested in tension using a micro-tensile testing rig. It is the intention of this study to measure the mechanical properties of this material at the micro-scale, and to evaluate the accuracy and reliability of micro-tensile testing for understanding the mechanical properties of the material. The conclusions arrived at in this study are as follows:

- The yield stress, ultimate tensile stress and strain hardening behaviour for the micron-scale tensile test are similar to those in macro-scale tensile tests. The results show micro-tensile testing can ascertain mechanical yielding behaviour representative of bulk macro scale behaviour, assuming the material has a cross-section area with more than 25 grains.
- The strain rate sensitivity measurements can be reproduced on a micron-scale, which yield values similar to macro scale tests.
- The elongation to failure of the micro-sized samples are smaller than the macro-size sample due to the presence of large (1.5 μm) and unwanted C and SiO_2 impurity particles present in the material. The study shows micro-tensile testing reaches its limitations where precipitates present are approaching half the size of the specimen diameter/width.
- Impurity particles introduced in the fabrication process of the Ni–SiC composite are found to be points of crack initiation and cause of the low elongation of this material. Grains located adjacent to impurity particles experience the greatest amount of deformation and fail by cleavage.
- The authors speculate that ductility of future batches of Ni–SiC composites might be improved through better raw material refinement and control of processing conditions.

Data availability

The raw/processed data required to reproduce these findings cannot be shared at this time as the data also forms part of an ongoing study.

Declaration of competing interest

The authors declare that they have no known competing financial interests or personal relationships that could have appeared to influence the work reported in this paper.

Acknowledgment

The authors would like to express their sincere gratitude to Tim Palmer and Kim Lu from the Nuclear Materials Development and Characterization group (NMDC) at ANSTO for their advice and help on sample preparation related issues. Also, thanks go to Colin Hobman from Maintenance Workshop at ANSTO. Sincere thanks are also due to Dr. Robert Wheeler of MicroTesting Solutions, OH, for many fruitful discussions and suggestions. This project was funded by internal research funding from the Nuclear Fuel Cycle Research division in ANSTO, the Shanghai Sailing Program under Project No. 18YF1428600 and internal funding from the Shanghai Institute of Applied Physics. The authors would also like to acknowledge Dr Hefei Huang and Dr Xingtai Zhou from SINAP and Dr Guoliang Zhu and Prof Baode Sun from SJTU.

Appendix 1. Plotting relationship between grip displacement vs strain

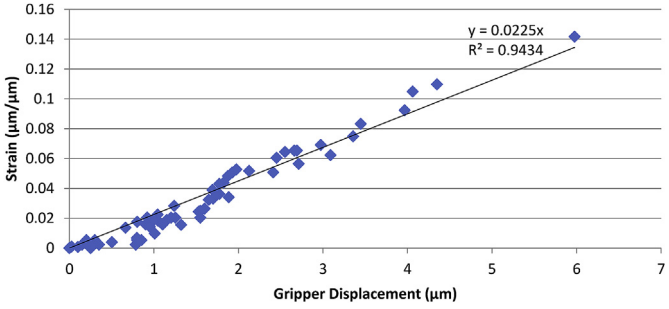

Appendix 2. Pole Figure Plots for two selected grains (circled in Red) Pre testing and at UTS.

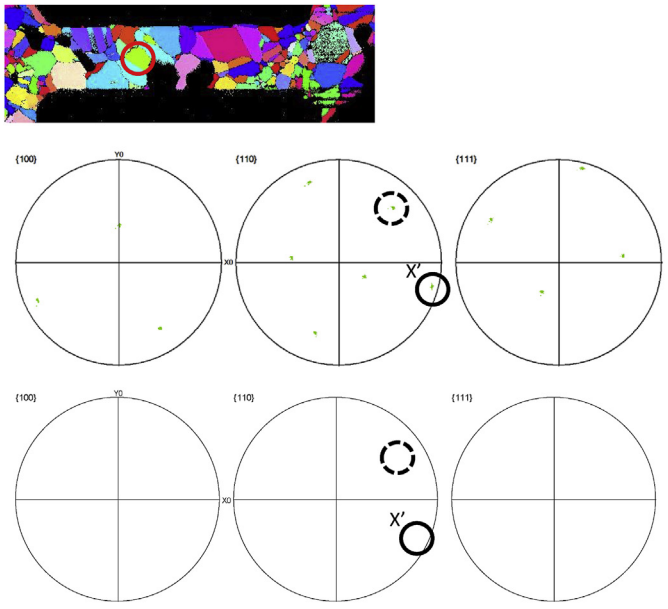

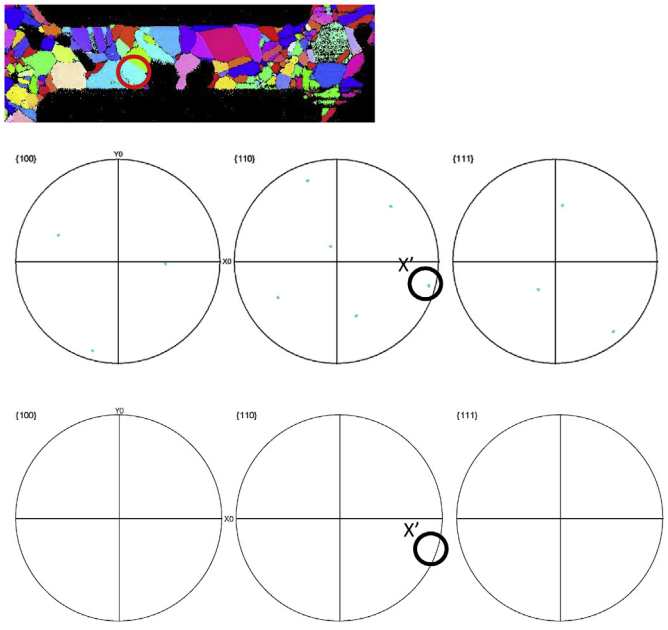

Appendix 3. TEM CBED analysis on carbon impurity (left image) and a matrix grain (right image) at same specimen orientation. No lattice spots or Kikuchi bands are present for the carbon impurity unlike the diffraction pattern for the grain which showed many lattice points and Kickuchi bands even when away from a zone axis.

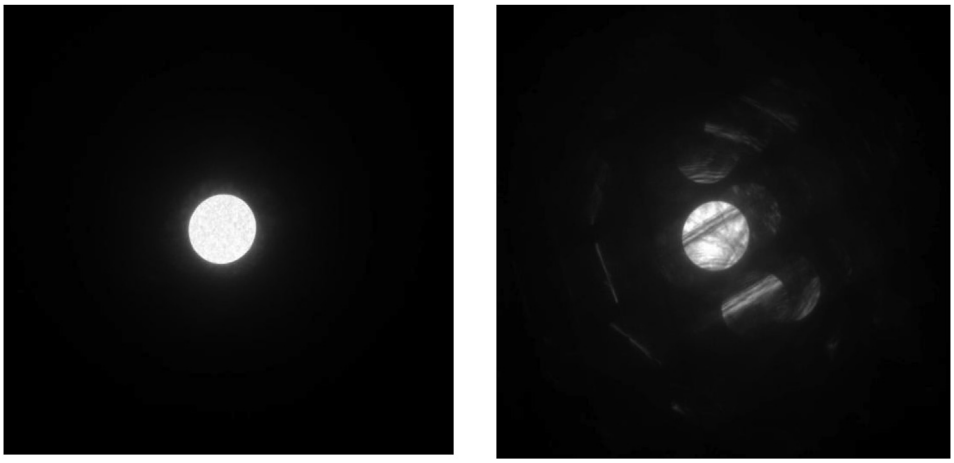

References

[1] D. LeBlanc, Molten salt reactors: a new beginning for an old idea, Nucl. Eng. Des. 240 (2010) 1644–1656, https://doi.org/10.1016/J.NUCENGDES.2009.12.033.

[2] M.M. Waldrop, Nuclear energy: radical reactors, Nature 492 (2012) 26–29, https://doi.org/10.1038/492026a.

[3] R.W. Moir, E. Teller, Thorium-fueled underground power plant based on molten salt Technology, Nucl. Technol. 151 (2005) 334–340, https://doi.org/10.13182/NT05-A3655.

[4] L. Mathieu, D. Heuer, R. Brissot, C. Garzenne, C. Le Brun, D. Lecarpentier, E. Liatard, J.-M. Loiseaux, O. Méplan, E. Merle-Lucotte, A. Nuttin, E. Walle, J. Wilson, The thorium molten salt reactor: moving on from the MSBR, Prog. Nucl. Energy 48 (2006) 664–679, https://doi.org/10.1016/J.PNUCENE.2006.07.005.

[5] K. Yabuuchi, N. Tsuda, A. Kimura, Y. Morisada, H. Fujii, H. Serizawa, S. Nogami, A. Hasegawa, T. Nagasaka, Effects of tool rotation speed on the mechanical properties and microstructure of friction stir welded ODS steel, Mater. Sci. Eng. A 595 (2014) 291–296, https://doi.org/10.1016/J.MSEA.2013.12.022.

[6] D. Bhattacharyya, P. Dickerson, G.R. Odette, S.A. Maloy, A. Misra, M.A. Nastasi, On the structure and chemistry of complex oxide nanofeatures in nano-structured ferritic alloy U14YWT, Philos. Mag. 92 (2012) 2089–2107, https://doi.org/10.1080/14786435.2012.662760.

[7] S. Chen, Y. Wang, N. Hashimoto, S. Ohnuki, Post-irradiation annealing behavior of helium in irradiated Fe and ferritic-martensitic steels, Nucl. Mater. Energy. 15 (2018) 203–207, https://doi.org/10.1016/J.NME.2018.04.012.

[8] N. Oono, S. Ukai, S. Kondo, O. Hashitomi, A. Kimura, Irradiation effects in oxide dispersion strengthened (ODS) Ni-base alloys for Gen. IV nuclear reactors, J. Nucl. Mater. 465 (2015) 835–839, https://doi.org/10.1016/J.JNUCMAT.2015.06.057.

[9] B. El-Dasher, J. Farmer, J. Ferreira, M.S. de Caro, A. Rubenchik, A. Kimura, Corrosion of oxide dispersion strengthened iron–chromium steels and tantalum in fluoride salt coolant: an in situ compatibility study for fusion and fusion–fission hybrid reactor concepts, J. Nucl. Mater. 419 (2011) 15–23, https://doi.org/10.1016/J.JNUCMAT.2011.07.036.

[10] C. Yang, H.-F. Huang, M. de los Reyes, L. Yan, X.-T. Zhou, T. Xia, D.-L. Zhang, Microstructures and tensile properties of ultrafine-grained Ni–(1–3.5) wt% SiCNP composites prepared by a powder metallurgy route, Acta Metall. Sin. (English Lett.) 28 (2015) 809–816, https://doi.org/10.1007/s40195-015-0261-5.

[11] H. Huang, C. Yang, M. de los Reyes, Y. Zhou, L. Yan, X. Zhou, Effect of milling time on the microstructure and tensile properties of ultrafine grained Ni–SiC composites at room temperature, J. Mater. Sci. Technol. 31 (2015) 923–929, https://doi.org/10.1016/J.JMST.2014.12.009.

[12] C. Yang, H. Huang, X. Zhou, Z. Li, X. Zhou, T. Xia, D. Zhang, High-temperature stability of Ni-3 wt.% SiCNP composite and the effect of milling time, J. Nucl. Mater. 467 (2015) 635–643, https://doi.org/10.1016/J.JNUCMAT.2015.10.044.

[13] H.F. Huang, W. Zhang, M. De Los Reyes, X.L. Zhou, C. Yang, R. Xie, X.T. Zhou, P. Huai, H.J. Xu, Mitigation of He embrittlement and swelling in nickel by dispersed SiC nanoparticles, Mater. Des. 90 (2016) 359–363, https://doi.org/10.1016/j.matdes.2015.10.147.

[14] X.L. Zhou, H.F. Huang, R. Xie, G.J. Thorogood, C. Yang, Z.J. Li, H.J. Xu, Helium ion irradiation behavior of Ni-1wt.%SiCNP composite and the effect of ion flux, J. Nucl. Mater. 467 (2015) 848–854, https://doi.org/10.1016/j.jnucmat.2015.11.004.

[15] S.J. Zinkle, L.L. Snead, Opportunities and limitations for ion beams in radiation effects studies: bridging critical gaps between charged particle and neutron irradiations, Scr. Mater. 143 (2018) 154–160, https://doi.org/10.1016/j.scriptamat.2017.06.041.

[16] P. Hosemann, Small-scale mechanical testing on nuclear materials: bridging the experimental length-scale gap, Scr. Mater. 143 (2018) 161–168, https://doi.org/10.1016/j.scriptamat.2017.04.026.

[17] A. Reichardt, M. Ionescu, J. Davis, L. Edwards, R.P. Harrison, P. Hosemann, D. Bhattacharyya, In situ micro tensile testing of He+2 ion irradiated and implanted single crystal nickel film, Acta Mater. 100 (2015) 147–154, https://doi.org/10.1016/j.actamat.2015.08.028.

[18] D. Bhattacharyya, R.W. Wheeler, R.P. Harrison, L. Edwards, The observation of slip phenomena in single crystal Fe samples during in situ micro-mechanical testing through orientation imaging, Microsc. Microanal. 20 (2014) 1060–1069, https://doi.org/10.1017/S1431927614001640.

[19] C.D. Hardie, C.A. Williams, S. Xu, S.G. Roberts, Effects of irradiation temperature and dose rate on the mechanical properties of sel-fion implanted Fe and Fe-Cr alloys, J. Nucl. Mater. 439 (2013) 33–40.

[20] D.E.J. Armstrong, X. Yi, E.A. Marquis, S.G. Roberts, Hardening of self ion implanted tungsten and tungsten 5-wt% rhenium, J. Nucl. Mater. 432 (2013) 428–436.

[21] Y. Kihara, T. Nagoshi, T.-F.M. Chang, H. Hosoda, S. Tatsuo, M. Sone, Tensile behavior of micro-sized specimen made of single crystalline nickel, Mater. Lett. 153 (2015) 36–39, https://doi.org/10.1016/j.matlet.2015.03.119.

[22] H.T. Vo, A. Reichardt, D. Frazer, N. Bailey, P. Chou, P. Hosemann, In situ micro-tensile testing on proton beam-irradiated stainless steel, J. Nucl. Mater. 493 (2017) 336–342, https://doi.org/10.1016/j.jnucmat.2017.06.026.

[23] A. Xu, M. Saleh, J. Davis, L. Edwards, D. Bhattacharyya, In-situ micro-tensile investigation of strain rate response along <100> and <110> directions in single crystal nickel, Int. J. Plast. 106 (2018) 129–144, https://doi.org/10.1016/j.ijplas.2018.03.005.

[24] B. Yang, C. Motz, M. Rester, G. Dehm, Yield stress influenced by the ratio of wire diameter to grain size – a competition between the effects of specimen microstructure and dimension in micro-sized polycrystalline copper wires, Philos. Mag. 92 (2012) 3243–3256, https://doi.org/10.1080/14786435.2012.693215.

[25] C. Yang, H. Huang, G.J. Thorogood, L. Jiang, X. Ye, Z. Li, X. Zhou, The effect of grain size and dislocation density on the tensile properties of Ni-SiCNP composites during annealing, J. Mater. Eng. Perform. 25 (2016) 726–733, https://doi.org/10.1007/s11665-016-1938-2.
[26] E.O. Hall, Yield Point Phenomena in Metals and Alloys, Springer US, 1970.
[27] A.J. Schwartz, M. Kumar, B.L. Adams, D.P. Field, , (n.d).
[28] C. WANG, C. WANG, J. XU, P. ZHANG, D. SHAN, B. GUO, Z. WANG, Tensile deformation behaviors of pure nickel fine wire with a few grains across diameter, Trans. Nonferrous Metals Soc. China 26 (2016) 1765–1774, https://doi.org/10.1016/S1003-6326(16)64287-5.
[29] C. Wang, C. Wang, J. Xu, P. Zhang, D. Shan, B. Guo, Plastic deformation size effects in micro-compression of pure nickel with a few grains across diameter, Mater. Sci. Eng. A 636 (2015) 352–360, https://doi.org/10.1016/j.msea.2015.03.087.
[30] G.E. Dieter, D.J. Bacon, Mechanical Metallurgy, McGraw-Hill, 1988.
[31] R.T. Humphrey, A.F. Jankowski, Strain-rate sensitivity of strength in macro-to-micro-to-nano crystalline nickel, Surf. Coat. Technol. 206 (2011) 1845–1849, https://doi.org/10.1016/j.surfcoat.2011.08.010.
[32] R. Schwaiger, B. Moser, M. Dao, N. Chollacoop, S. Suresh, Some critical experiments on the strain-rate sensitivity of nanocrystalline nickel, Acta Mater. 51 (2003) 5159–5172, https://doi.org/10.1016/S1359-6454(03)00365-3.
[33] J. Luo, M.Q. Li, Strain rate sensitivity and strain hardening exponent during the isothermal compression of Ti60 alloy, Mater. Sci. Eng. A 538 (2012) 156–163, https://doi.org/10.1016/J.MSEA.2012.01.021.
[34] R. Abbaschian, L. Abbaschian, R.E. Reed-Hill, Physical Metallurgy Principles, fourth ed., Cengage Learning, USA, 2010.
[35] Y. Ding, J. Jiang, A. Shan, Plastic instability and strain rate sensitivity of ultrafine-grained iron, J. Alloy. Comp. 487 (2009) 517–521, https://doi.org/10.1016/J.JALLCOM.2009.08.004.
[36] X.W. Gu, C.N. Loynachan, Z. Wu, Y.-W. Zhang, D.J. Srolovitz, J.R. Greer, Size-dependent deformation of nanocrystalline Pt nanopillars, Nano Lett. 12 (2012) 6385–6392, https://doi.org/10.1021/nl3036993.
[37] G. Dehm, B.N. Jaya, R. Raghavan, C. Kirchlechner, Overview on micro- and nanomechanical testing: new insights in interface plasticity and fracture at small length scales, Acta Mater. 142 (2018) 248–282, https://doi.org/10.1016/j.actamat.2017.06.019.